RSC Advances

PAPER

View Article Online
View Journal | View Issue

Cite this: *RSC Adv.*, 2015, **5**, 30851

Hydrothermal synthesis of bismuth oxybromide–bismuth oxyiodide composites with high visible light photocatalytic performance for the degradation of CV and phenol†

Yu-Rou Jiang, Shang-Yi Chou, Jia-Lin Chang, Shiuh-Tsuen Huang, Ho-Pan Lin and Chiing-Chang Chen*

Received 28th January 2015
Accepted 18th March 2015

DOI: 10.1039/c5ra01702e

www.rsc.org/advances

This is the first report on a series of BiO_pBr_q/BiO_mI_n heterojunctions that were prepared using controlled hydrothermal methods. The compositions and morphologies of the BiO_pBr_q/BiO_mI_n could be controlled by adjusting some growth parameters, including reaction pH value, temperature, time, and KBr/KI molar ratio. The photocatalytic efficiency of the powder suspensions was evaluated by measuring crystal violet (CV) and phenol concentrations. Both the photocatalytic process and the photosensitized process were found to work concurrently. The quenching effects of various scavengers and EPR indicated that the reactive $O_2^{\bullet-}$ played a major role and $^{\bullet}OH$ and h^+ played minor roles. The photocatalytic activity of the BiO_pBr_q/BiO_mI_n heterojunctons reached the maximum rate constant of 0.5285 (or 0.4713) h^{-1}, 10 times higher than that of P25–TiO_2, 14 times higher than that of BiOBr, and 6 times higher than that of BiOI.

1. Introduction

The large amount of dyes used in the dyeing stage of textile manufacturing processes represents an increasing environmental danger due to their refractory carcinogenic nature. Particularly, triphenylmethane (TPM) dyes are consumed heavily in the leather, cosmetic, paper, and food industries for the coloring of plastics, oil, fats, waxes, and varnish.[1] The photocytotoxicity of TPM dyes, based on the production of reactive oxygen species, has been intensively studied with regard to photodynamic treatment.[2] However, there is a great concern about the thyroid peroxidase-catalyzed oxidation of TPM dyes because the reactions might form various *N*-dealkylated aromatic amines, whose structures are similar to aromatic amine carcinogens.[3] Cationic TPM dyes are widely used as antimicrobial agents. Recent reports indicated that they might further serve as targetable sensitizers in the photodestruction of specific cellular components or cells.[2,3] Photocatalysis has been successfully used for degrading TPM dye pollutants in the past few years.[4,5] In view of the efficient utilization of visible light, the development of new and efficient visible-light-driven photocatalysts remains a major challenge from the practical use and commercial viewpoints.

Recently, the development of visible-light-sensitive photocatalysts has received considerable attention as an alternative to wastewater treatment. An effective and simple strategy to improve the photocatalytic activity of a photocatalyst is the incorporation of a heterostructure (or composite), because heterojunctions (or composites) have great potential for tuning the desired electronic properties of composite photocatalysts and efficiently separating the photogenerated electron–hole pairs.[6–12] In recent years, a new family of promising photocatalysts, bismuth oxyhalides,[13–16] which belong to the V-VI-VII family of multi-component metal oxyhalides, have demonstrated remarkable photocatalytic activities due to their uniquely layered structures with an internal static electric field perpendicular to each layer, which can induce the effective separation of photogenerated electron–hole pairs. An effective and simple tactic to improve the photocatalytic activity of a photocatalyst is the architecture of the heterostructure, as the heterojunction has great potential for tuning the desired electronic properties of the composite photocatalysts and efficiently separating the photogenerated electron–hole pairs.[17] Xiao *et al.*[18] reported the synthesis of BiOI/BiOCl phases exhibiting high photocatalytic activities under visible light irradiation for the degradation of bisphenol-A, respectively. Cao *et al.*[19] developed a facile synthesis of BiOCl/BiOI by a sol–gel process.

This research reports the preparation and characterization of a series of BiO_pBr_q/BiO_mI_n photocatalysts. This is the first report demonstrating a systematic synthesis study on BiO_pBr_q/BiO_mI_n photocatalysts by autoclave hydrothermal methods. The photocatalytic activities of the BiO_pBr_q/BiO_mI_n photocatalysts

National Taichung University of Education, Department of Science Education and Application, Taichung, Taiwan. E-mail: ccchen@ms3.ntcu.edu.tw; ccchen@mail.ntcu.edu.tw

† Electronic supplementary information (ESI) available. See DOI: 10.1039/c5ra01702e

were evaluated by measuring the degradation rates of CV and phenol, and found to have excellent activity under visible light irradiation. In comparison to P25–TiO_2, the new photoactive material demonstrates a higher rate for removing aqueous CV under visible light irradiation.

2. Experimental

2.1 Materials

The purchased $Bi(NO_3)_3 \cdot 5H_2O$, KI (Katayama), KBr (Shimakyu), CV dye (TCI), *p*-benzoquinone (Alfa Aesar), sodium azide (Sigma), ammonium oxalate (Osaka), and isopropanol (Merck) were obtained and used without any further purification. Reagent-grade sodium hydroxide, nitric acid, ammonium acetate and HPLC-grade methanol were obtained from Merck.

2.2 Synthesis of BiO_pBr_q/BiO_mI_n

5 mmol Bi $(NO_3)_3 \cdot 5H_2O$ was first mixed in a 50 mL flask and then 5 mL of 4 M HNO_3 was added. With continuous stirring, 2 M NaOH was added dropwise to adjust the pH value and, when a precipitate formed, 2 mL of KBr and KI were also added dropwise. The solution was then stirred vigorously for 30 min and transferred into a 30 mL Teflon-lined autoclave, which was heated up to 110–260 °C for 12 h and then naturally cooled down to room temperature. The resulting solid precipitate was collected by filtration, washed with deionized water and methanol to remove any possible ionic species in the solid precipitate, and then dried at 60 °C overnight. Depending on the molar ratio of KBr to KI (2 : 1, 1 : 2), pH value, temperature, and time, different BiO_pBr_q/BiO_mI_n composites could be synthesized and were labeled as in Table S1 of the ESI,† namely BB1I2-1-110-12 (Br : I = 1 : 2; pH = 1; temp = 110 °C; time = 12 h) to BB2I1-13-260-12 (Br : I = 2 : 1; pH = 13; temp = 260 °C; time = 12 h) for the as-prepared samples, respectively.

2.3 Instruments and analytical methods

The products were characterized using XRD, FE-SEM-EDS, HRXPS, FE-TEM-EDS, CL, EPR, and BET. The intermediates formed during the decomposition process were isolated, identified, and characterized using HPLC-PDA-ESI-MS. The detailed conditions are described in the ESI.†

2.4 Photocatalytic activity test

An aqueous suspension of CV (100 mL, 10 ppm) and an amount of the catalyst powder were placed in a Pyrex flask. The pH value of the suspension was adjusted by adding either NaOH or HNO_3 solution. Prior to irradiation, the suspension was magnetically stirred in the dark for *ca.* 30 min to establish an adsorption/desorption equilibrium between the dye and the surface of the catalyst under ambient air-equilibrated conditions. The irradiation was carried out using visible-light lamps (150 W Xe arc). The light intensity was fixed at 32.1 Wm^{-2} when the reactor was placed 30 cm away from the light source. The irradiation experiments of CV were carried out on a stirring aqueous solution contained in a 100 mL flask. At the given irradiation time intervals, a 5 mL aliquot was collected and centrifuged to remove the catalyst. The supernatant was analyzed by HPLC-ESI-MS after readjusting the chromatographic conditions in order to make the mobile phase compatible with the working conditions of the mass spectrometer.

3. Results and discussion

3.1 Phase structure

Fig. 1 and S1–S7 (ESI†) show the XRD patterns of the as-prepared BiO_pBr_q/BiO_mI_n samples. The XRD patterns clearly reveal the coexistence of different phases. All the BiO_pBr_q/BiO_mI_n samples prepared using the described hydrothermal method at different temperatures and pH contain the BiOBr (JCPDS 09-0393), $Bi_4O_5Br_2$ (JCPDS 37-0669), $Bi_{24}O_{31}Br_{10}$ (JCPDS 75-0888), Bi_3O_4Br (JCPDS 84-0793), Bi_5O_7Br (JCPDS 38-0493), $Bi_{12}O_{17}Br_2$ (JCPDS 37-0701), BiOI (JCPDS 73-2062), $Bi_7O_9I_3$,[20,21] and Bi_5O_7I (JCPDS 40-0548) phases. The XRD patterns for pH = 1, 4, 7, 10, and 13 are identical to those reported for the BiOI single phase, the BiOBr/BiOI, $Bi_3O_4Br/Bi_7O_9I_3$, Bi_5O_7Br/Bi_5O_7I, $Bi_{24}O_{31}Br_{10}$/BiOI, Bi_3O_4Br/Bi_5O_7I binary phase, and the BiOBr/$Bi_{24}O_{31}Br_{10}$/BiOI, BiOBr/$Bi_4O_5Br_2$/BiOI ternary phases. Table 1 summarizes the results of the XRD measurements.

Fig. 2–4 display that BB1I2-4-210-12, BB2I1-4-110-12, and BB1I2-4-110-12 are composed of sheets or plates with different sizes, consistent with the TEM observation. In addition, the EDS spectrum shows the sample contains Bi, O, Br and I elements. The TEM-EDS results show that the main elements of these samples are bismuth, iodine, chlorine, and oxygen. The Br (or I) atomic ratio (%) of the samples is within the range of 3.86–7.83 (or 9.55–15.37), corresponding to different heterojunctions. The

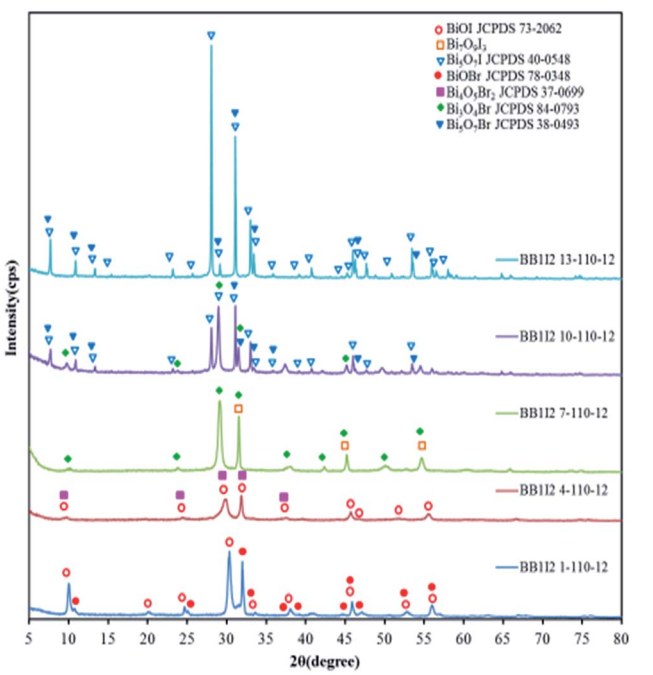

Fig. 1 XRD patterns of the as-prepared BiO_pBr_q/BiO_mI_n samples under different pH values. (Molar ratio KBr/KI = 1/2, hydrothermal conditions: temp = 110 °C, pH = 1–13, time = 12 h).

Table 1 Crystalline phase changes of the binary bismuth oxyhalide nanosheets prepared under different reaction conditions (●BiOBr; ■$Bi_4O_5Br_2$; ▲$Bi_{24}O_{31}Br_{10}$; ◆Bi_3O_4Br; ●$Bi_{12}O_{17}Br_2$; ▼Bi_5O_7Br; ○BiOI; □$Bi_7O_9I_3$; ▽Bi_5O_7I)

	Temp (°C)			
pH	110	160	210	260
BB1I2				
1	■○	■○	■○	■○
4	■○	■○	■○	■▲○
7	◆□	◆□	◆□	◆□
10	▼▽	▼▽	◆▽	▼▽
13	▼▽	▼▽	▼▽	▼▽
BB2I1				
1	●○	●○	●○	●
4	■○	■○	■▲○	■▲○
7	●■○	●■○	▲○	▲○
10	◆▽	◆▽	◆▽	◆▽
13	▼▽	▼▽	▼▽	▼▽

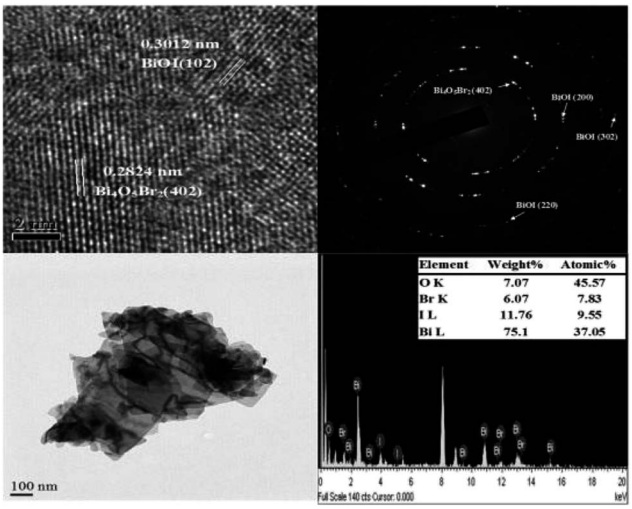

Fig. 2 FE-TEM images and EDS of the BB1I2-4-210-12 sample prepared by the hydrothermal autoclave method.

HRTEM image reveals that two sets of different lattice images are found with the *d* spacing of 0.2824 and 0.3012 nm, corresponding to the (4 0 2) plane of $Bi_4O_5Br_2$ and the (1 0 2) plane of BiOI (Fig. 2), 0.2814 and 0.2824 nm, corresponding to the (0 2 0) plane of $Bi_4O_5Br_2$ and the (1 1 0) plane of BiOI (Fig. 3), and 0.2836 and 0.2812 nm, corresponding to the (1 2 0) plane of $Bi_4O_5Br_2$ and the (1 1 0) plane of BiOI (Fig. 4), respectively, which is in good accordance with the results of the XRD patterns. The results suggest that Bi_4O_5Br/BiOI has formed in

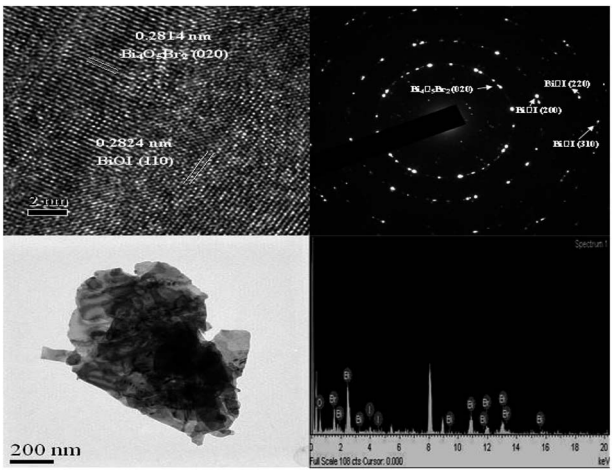

Fig. 3 FE-TEM images and EDS of the BB2I1-4-110-12 sample prepared by the hydrothermal autoclave method.

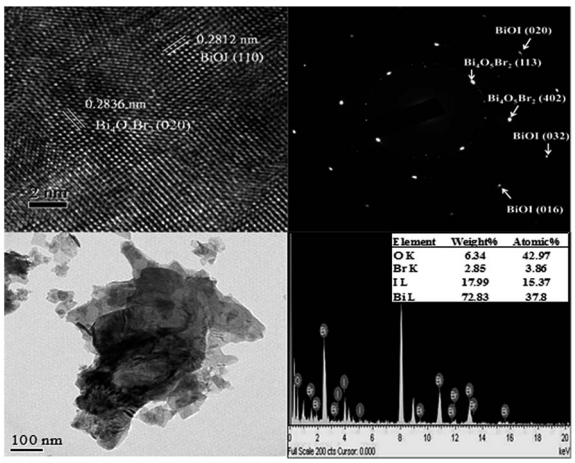

Fig. 4 FE-TEM images and EDS of the BB1I2-4-110-12 sample prepared by the hydrothermal autoclave method.

the composites, which will favor the separation of the photo-induced carriers and thus acquire high photocatalytic activities.

In this experiment, the pH value plays a major role in controlling the composition and anisotropic growth of the crystals. The results show that a series of changes in the compounds occur at different pH values of the hydrothermal reactions, described as BiOBr → $Bi_4O_5Br_2$ → $Bi_{24}O_{31}Br_{10}$ → Bi_3O_4Br → Bi_5O_7Br → $Bi_{12}O_{17}Br_2$ → α-Bi_2O_3 and BiOI → $Bi_4O_5I_2$ → $Bi_7O_9I_3$ → Bi_3O_4I → Bi_5O_7I → α-Bi_2O_3. The possible processes for the formation of the BiO_pBr_q/BiO_mI_n samples are described as follows [eqn (1)–(18)].

$$Bi^{3+} + 3OH^- \rightarrow Bi(OH)_{3(s)} \quad (1)$$

$$2Bi(OH)_{3(s)} + Br^- \rightarrow BiOBr_{(s)} + H_2O + OH^- \quad (2)$$

$$Bi^{3+} + 3Br^- \rightarrow BiBr_{3(s)} \quad (3)$$

$$BiBr_{3(s)} + 2OH^- \rightarrow BiOBr_{(s)} + 2Br^- + H_2O \quad (4)$$

$$4BiOBr_{(s)} + 2OH^- \rightarrow Bi_4O_5Br_{2(s)} + 2Br^- + H_2O \quad (5)$$

$$6Bi_4O_5Br_{2(s)} + 2OH^- \rightarrow Bi_{24}O_{31}Br_{10(s)} + 2Br^- + H_2O \quad (6)$$

$$Bi_{24}O_{31}Br_{10(s)} + 2OH^- \rightarrow 8Bi_3O_4Br_{(s)} + 2Br^- + H_2O \quad (7)$$

$$5Bi_3O_4Br_{(s)} + 2OH^- \rightarrow 3Bi_5O_7Br_{(s)} + 2Br^- + H_2O \quad (8)$$

$$12Bi_5O_7Br_{(s)} + 2OH^- \rightarrow 5Bi_{12}O_{17}Br_{2\ (s)} + 2Br^- + H_2O \quad (9)$$

$$Bi_{12}O_{17}Br_{2(s)} + 2OH^- \rightarrow 6Bi_2O_{3(s)} + 2Br^- + H_2O \quad (10)$$

$$2Bi(OH)_{3(s)} + I^- \rightarrow BiOI_{(s)} + H_2O + OH^- \quad (11)$$

$$Bi^{3+} + 3^- \rightarrow BiI_{3(s)} \quad (12)$$

$$BiI_{3(s)} + 2OH^- \rightarrow BiOI_{(s)} + 2I^- + H_2O \quad (13)$$

$$4BiOI_{(s)} + 2OH^- \rightarrow Bi_4O_5I_{2(s)} + 2I^- + H_2O \quad (14)$$

$$7Bi_4O_5I_{2(s)} + 2OH^- \rightarrow 4Bi_7O_9I_{3(s)} + 2I^- + H_2O \quad (15)$$

$$3Bi_7O_9I_{3(s)} + 2OH^- \rightarrow 7Bi_3O_4I_{(s)} + 2I^- + H_2O \quad (16)$$

$$5Bi_3O_4I_{(s)} + 2OH^- \rightarrow 3Bi_5O_7I_{(s)} + 2I^- + H_2O \quad (17)$$

$$2Bi_5O_7I_{(s)} + 2OH^- \rightarrow 5Bi_2O_{3(s)} + 2I^- + H_2O \quad (18)$$

These equations show that BiOBr (or BiOI) is formed at the beginning of the reaction, and then OH^- gradually substitutes Br^- (or I^-) in basic conditions, resulting in the reduced content of Br^- (or I^-) in the products. With increasing pH, BiOBr, $Bi_4O_5Br_2$, $Bi_{24}O_{31}Br_{10}$, Bi_3O_4Br, Bi_5O_7Br, $Bi_{12}O_{17}Br_2$, and BiOI, $Bi_4O_5I_2$, $Bi_7O_9I_3$, Bi_3O_4I, Bi_5O_7I, and α-Bi_2O_3 could be obtained gradually. The higher pH value reveals the lower Br^- (or I^-) content in the products, until the content of Br^- (or I^-) in the products is fully replaced by OH^-, finally resulting in the formation of α-Bi_2O_3 under strongly basic conditions. A competitive relationship typically exists among the OH^-, Br^-, and I^- ions in the aqueous solution. It is demonstrated that a different BiO_pBr_q/BiO_mI_n can be selectively prepared through adjusting the pH value under the hydrothermal method.

3.2 Morphological structure and composition

The surface morphology of the BiO_pBr_q/BiO_mI_n was examined by FE-SEM-EDS (Fig. S8 and S9, ESI†). From Table 2, the EDS results show that the main elements of these samples are bismuth, bromine, iodine, and oxygen under different pH values. The detailed morphological structure and composition are described in the ESI.†

3.3 XPS analysis

XPS was employed to examine the purity of the prepared BiO_pBr_q/BiO_mI_n products, and the spectra are shown in Fig. 5 and 6. Fig. 5 shows the total survey spectra of Bi 4f, Br 3d, I 3d, and O 1s XPS of the five BiO_pBr_q/BiO_mI_n samples. According to Fig. 5(a), the observation of transition peaks involving the Bi 4f, Br 3d, I 3d, O 1s, and C 1s orbitals reveals that the catalysts are constituted by the elements Bi, O, Br, I, and C. The characteristic binding energy value of 158.1–158.9 eV for Bi $4f_{7/2}$ (Fig. 5(b)) reveals a trivalent oxidation state for bismuth. An additional spin–orbit doublet with the binding energy of 155.7–156.3 eV for Bi $4f_{7/2}$ was also observed in all samples, suggesting that certain parts of bismuth exist in the $(+3 - x)$ valence state. This indicates that the trivalent bismuth is partially reduced to the lower valence state by the hydrothermal autoclave method. A similar chemical shift of approximately 2.4–2.6 eV for Bi $4f_{7/2}$ was also observed by Chen *et al.*[5] They concluded that the $Bi^{(+3-x)}$ formal oxidation state could most probably be attributed to the substoichiometric forms of Bi within the Bi_2O_2 layer and the formation of the low oxidation state resulted in oxygen vacancies in the crystal lattice. However, it was assumed that the $Bi^{(+3-x)}$ formal oxidation state could most likely be attributed to the substoichiometric forms of Bi at the outer site of the particles and the formation of the low oxidation state resulted in oxygen vacancies in the crystal surface. Fig. 5(c) shows the high-resolution XPS spectra for the O 1s region, which can be fitted into two peaks. The main peak at 529.1 eV is attributed to the Bi–O bonds in the $(Bi_2O_2)^{2+}$ slabs of the BiOX layered structure, and the peak at 530.9 eV is assigned to the hydroxyl groups on the surface.[15] From Fig. 5(d), the binding energies of 67.4–67.8 eV and 68.5–68.9 eV are attributed to the Br $3d_{5/2}$ and $3d_{3/2}$ respectively which can be assigned to Br in the monovalent oxidation state. The binding energies of 617.8–618.7 eV and 629.5–630.2 eV are attributed to I $3d_{5/2}$ and $3d_{3/2}$ respectively, which can be assigned to I in the monovalent oxidation state (Fig. 5(e)). In the Bi_2O_3 (BB3-1-110-12 (BiOBr) or BI3-1-110-12 (BiOI)) samples, two sets of peaks centered at 164.0 and 158.5 (164.2 and 158.7 or 163.5 and 158.1) eV can be attributed to Bi $4f_{5/2}$ and Bi $4f_{7/2}$, demonstrating that the main chemical states of the bismuth element in the samples is trivalent. The characteristic binding energy reveals a trivalent oxidation state for the Bi^{+3}–O (Bi^{+3}–Br or Bi^{+3}–I) bonding. Two additional spin–orbit doublets with the binding energy for Bi $4f_{7/2}$ are also observed, suggesting that certain parts of bismuth exist in the Bi^{+3-x}–O (Bi^{+3-x}–Br or Bi^{+3-x}–I) bonding.[5] The XPS results reveal that the possible processes for the formation of bismuth oxybromoiodides are described as eqn (1)–(18), which are consistent with the previous results by XRD and TEM analyses. Besides, the results show that the main elements of these samples are bismuth, bromine, iodine, and oxygen from Table 2. The Br (or I) atomic ratio (%) of the samples is within the range of 0.4–8.8 (or 0.5–3.9), corresponding to different BiO_pBr_q/BiO_mI_n composites.

3.4 Photophysical properties of the new photocatalysts

The UV-vis diffuse reflectance spectra of the different catalysts are shown in Fig. 7(a). It can be observed that BiOBr absorbs visible light slightly while the absorption edge of BiOI extends to the whole spectrum of visible light. Moreover, the absorption edges of the BiO_pBr_q/BiO_mI_n composites have a monotonic red shift response of BiO_pBr_q. Based on the absorption spectra, the E_g of the semiconductor can be calculated from the $\alpha h\nu = A(h\nu - E_g)^{n/2}$ equation.[19,22] The values of n for BiOBr and BiOI are

Table 2 Physical and chemical properties of BiO_pBr_q/BiO_mI_n

	EDS of atomic ratio (%)				XPS of atomic ratio (%)				
Catalyst code	Bi	O	Br	I	Bi	O	Br	I	E_g (eV)
BB1I2-1-110-12	31.64	39.72	11.04	17.59	70.9	16.3	8.8	3.9	1.58
BB1I2-4-110-12	25.35	54.35	7.52	12.78	89.2	5.1	2.4	3.3	1.80
BB1I2-7-110-12	33.80	52.00	2.77	11.43	88.8	9.0	0.8	1.4	1.97
BB1I2-10-110-12	31.29	59.85	1.11	7.75	85.2	11.9	0.8	2.1	2.18
BB1I2-13-110-12	36.25	57.06	0.06	6.63	59.2	37.0	0.4	3.5	2.56
BB2I1-1-110-12	24.03	48.33	19.21	8.44	77.8	12.6	8.4	1.2	1.68
BB2I1-4-110-12	31.22	48.18	13.30	7.30	81.7	11.5	5.0	1.7	1.90
BB2I1-7-110-12	30.23	50.52	12.97	6.27	79.0	15.4	4.8	0.9	1.83
BB2I1-10-110-12	33.49	55.41	5.58	5.52	72.2	22.9	3.2	1.7	2.16
BB2I1-13-110-12	32.80	58.33	1.23	7.64	65.9	31.1	2.4	0.5	2.38
BB3-1-110-12	28.54	45.45	26.00	—	59.5	22.0	18.5	—	2.61
BI3-1-110-12	24.47	50.22	—	25.31	80.3	11.9	—	7.8	1.59

4 and 4, respectively. The E_g of BiO_pBr_q/BiO_mI_n was determined from a plot of $(\alpha h\nu)^{1/2}$ *vs.* energy ($h\nu$) in Fig. 7(b) and elicited to be 1.58–2.56 eV in Table 2. The difference of the band gap energies in the as-prepared BiO_pBr_q/BiO_mI_n can be ascribed to their individual composition with various characteristics. The steep shape and strong absorption in the visible region ascribe the visible light absorption to the intrinsic band gap transition between the valence band and the conduction band, rather than the transition from the impurity levels.[22]

3.5 Specific surface areas and pore structure

Fig. S10(a) of the ESI† shows the nitrogen adsorption–desorption isotherm curves of the BiO_pBr_q/BiO_mI_n samples for different pH values. The isotherms of all the samples are close to type IV (Brunauer–Deming–Deming–Teller, BDDT, classification) with a hysteresis loop at a high relative pressure between 0.6 and 1.0.[23] From Fig. S10(b) of the ESI,† the shape of the hysteresis loop is close to Type H3, suggesting the existence of slit-like pores generally formed by the aggregation of plate-like particles, which is consistent with the self-assembled nanoplate-like morphology of the samples.[23]

In Table S2 of the ESI,† BB1I2-4-110-12 and BB2I1-4-110-12 also have the larger BET value and pore volume. Thus, the large BET value and pore volume of the BiO_pBr_q/BiO_mI_n composites may play a role in enhancing the photocatalytic activity. The detailed BET and pore structure are described in the ESI.†

3.6 Photocatalytic activity

The changes in the UV-vis spectra during the photodegradation process of CV and phenol in the aqueous BiO_pBr_q/BiO_mI_n dispersions under visible light irradiation are illustrated in Fig. S12 of the ESI.† The degradation efficiency as a function of reaction time is illustrated in Fig. S13 of the ESI.† The removal efficiency is enhanced significantly in the presence of BiO_pBr_q/BiO_mI_n catalysts. After 48 h of irradiation, BiO_pBr_q/BiO_mI_n shows superior photocatalytic performance, with the CV removal efficiency up to 99%. To further understand the reaction kinetics of CV degradation, the apparent pseudo-first-order model[24] expressed by the $\ln(C_o/C) = k_{app}t$ equation was applied in these experiments. *Via* the first-order linear fit from the data of Fig. S13† shown in Table 3, k_{app} of BB1I2-4-110-12 was obtained at the maximal degradation rate of 5.285×10^{-1} h^{-1}, greatly higher than the other composites. Therefore, the $Bi_4O_5Br_2$/BiOI composite shows the best photocatalytic activity. The result shows that the $Bi_4O_5Br_2$/BiOI composite is a much more effective photocatalyst than the others. The superior photocatalytic ability of BiO_pBr_q/BiO_mI_n may be ascribed to its efficient utilization of visible light and the high separation efficiency of the electron–hole pairs with its composites.

The durability of the $Bi_4O_5Br_2$/BiOI (BB1I2-4-210-12) composite was evaluated through recycling the used catalyst. There was no apparent loss of photocatalytic activity for removing crystal violet in the fifth cycle, and even in the tenth run, the declination in photocatalytic activity was less than 3% (Fig. 8(a)). The used $Bi_4O_5Br_2$/BiOI was also examined by XRD, and there was no detectable difference between the as-prepared and used samples (Fig. 8(b)). Therefore, it can be deduced that the $Bi_4O_5Br_2$/BiOI composite has good photostability.

3.7 Cathodoluminescence spectrum

To investigate the separation capacity of the photogenerated carriers in the heterostructures, the CL spectra of BiOBr, BiOI, and BiO_pBr_q/BiO_mI_n were measured and the results are given in Fig. 9 The characteristic emission peak around 2.01 eV nearly disappears for the BiO_pBr_q/BiO_mI_n heterostructure, indicating that the recombination of photogenerated charge carriers is inhibited greatly. The efficient charge separation could increase the lifetime of the charge carriers and enhance the efficiency of the interfacial charge transfer to the adsorbed substrates, and then improve the photocatalytic activity.

3.8 Separation and identification

With visible irradiation, temporal variations occurring in the solution of the CV dye during the degradation process were examined by HPLC-PDA-MS. Given the CV irradiation up to 24 h at pH 4, the chromatograms are illustrated in Fig. S14 of the ESI† and were recorded at 580, 350, and 300 nm, and nineteen

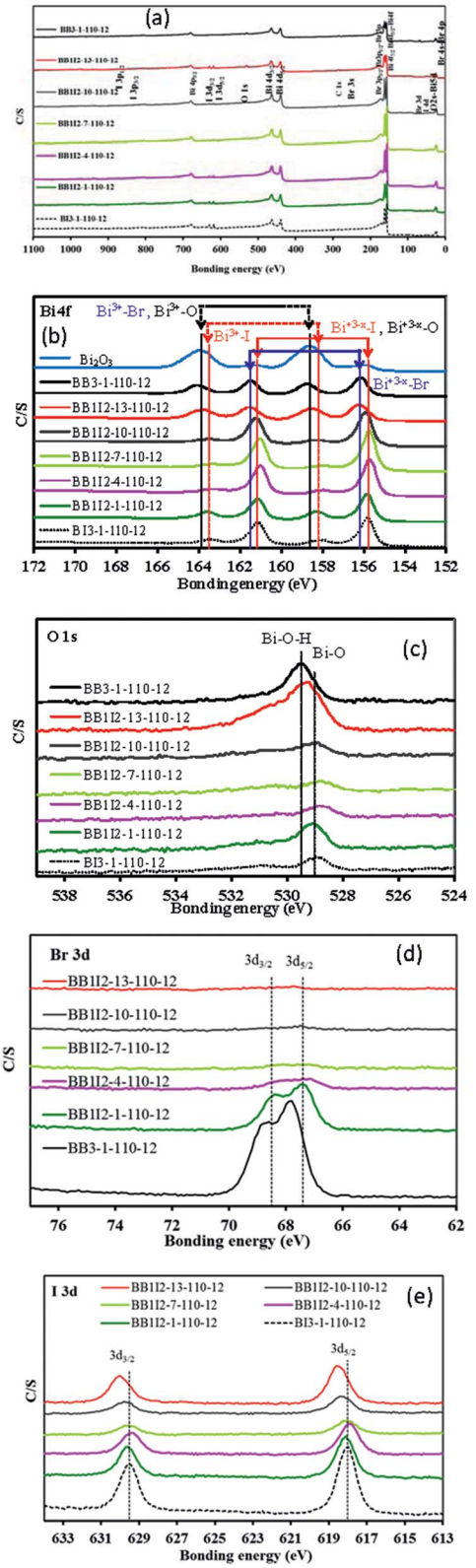

Fig. 5 High resolution XPS spectra of the as-prepared BiO_pBr_q/BiO_mI_n samples under different pH values. (a) total survey; (b) Bi 4f; (c) O 1s; (d) Br 3d; (e) I 3d. (Molar ratio KBr/KI = 1/2.)

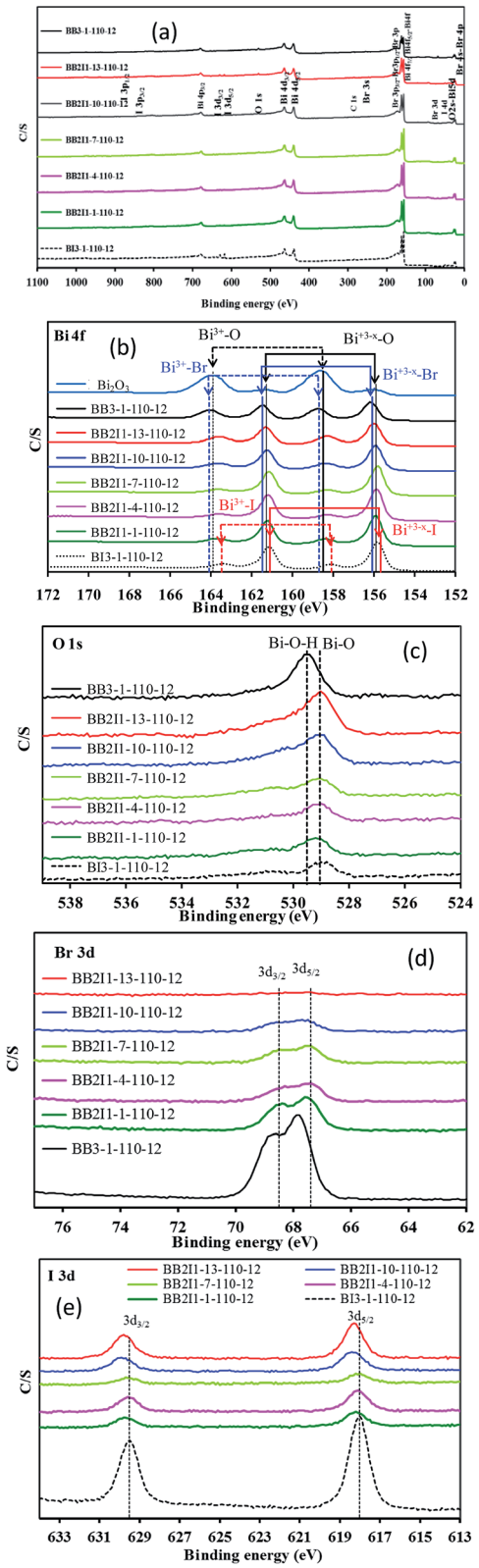

Fig. 6 High resolution XPS spectra of the as-prepared BiO_pBr_q/BiO_mI_n samples under different pH values. (a) total survey; (b) Bi 4f; (c) O 1s; (d) Br 3d; (e) I 3d. (Molar ratio KBr/KI = 2/1).

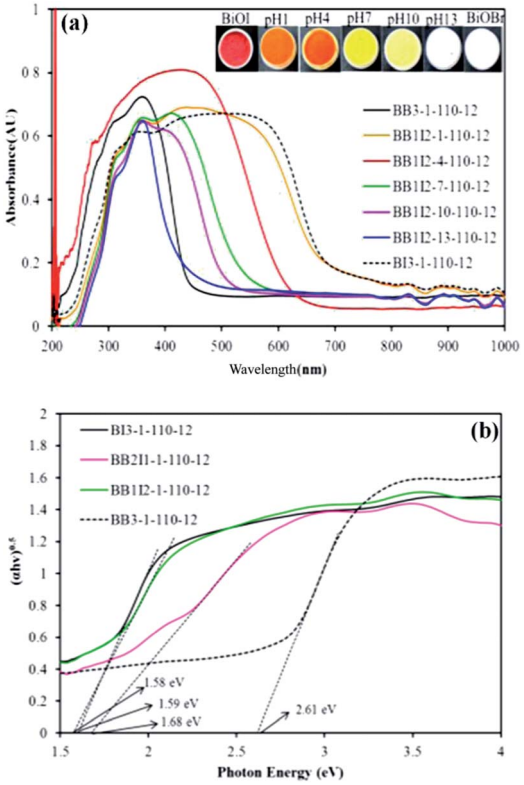

Fig. 7 UV–vis absorption spectra of the as-prepared BiO_pBr_q/BiO_mI_n samples under different (a) pH values and (b) molar ratios.

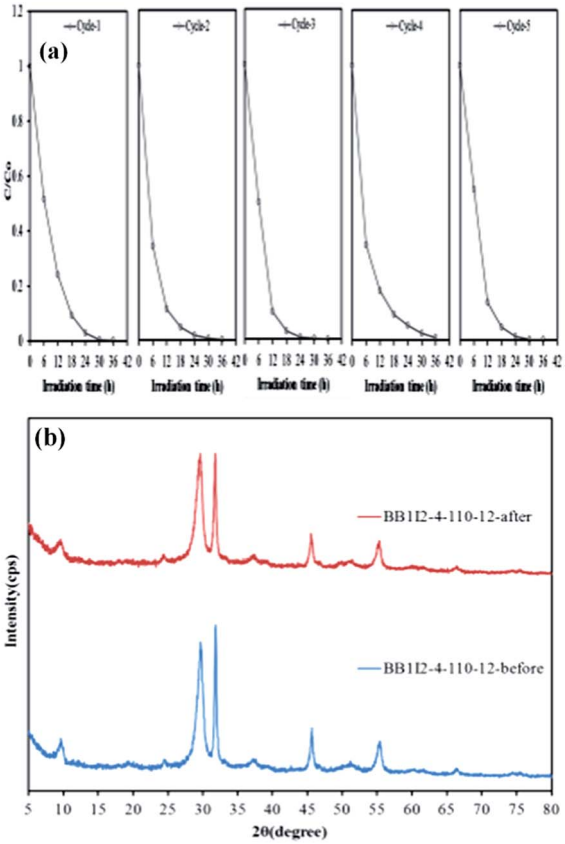

Fig. 8 (a) Cycling runs and (b) XRD patterns acquired before and after the photocatalytic degradation of CV in the presence of BB1I2-4-110-12.

Table 3 The pseudo-first-order rate constants for the degradation of CV with the BiO_pBr_q/BiO_mI_n photocatalysts under visible light irradiation

	Temp (°C)							
	110		160		210		260	
pH	k (h^{-1})	R^2	k (h^{-1})	R^2	k (h^{-1})	R^2	k (h^{-1})	R^2
BB1I2 series								
1	0.171	0.96	0.137	0.95	0.185	0.96	0.100	0.97
4	0.374	0.95	0.323	0.96	0.528	0.99	0.239	0.99
7	0.064	0.97	0.126	0.99	0.080	0.96	0.106	0.96
10	0.129	0.97	0.201	0.95	0.077	0.95	0.189	0.96
13	0.013	0.96	0.029	0.97	0.042	0.96	0.022	0.96
BB2I1 series								
1	0.143	0.97	0.139	0.96	0.249	0.96	0.025	0.98
4	0.471	0.96	0.427	0.96	0.416	0.97	0.310	0.98
7	0.243	0.97	0.398	0.96	0.103	0.97	0.086	0.98
10	0.143	0.96	0.094	0.96	0.087	0.98	0.064	0.93
13	0.009	0.97	0.002	0.98	0.010	0.98	0.020	0.94

BiOBr		BiOI		TiO_2	
k (h^{-1})	R^2	k (h^{-1})	R^2	k (h^{-1})	R^2
0.037	0.97	0.093	0.99	0.057	0.99

intermediates were identified, with the retention time of under 50 min. The CV dye and its related intermediates are denoted as species A–J, a–f, and α–γ. Except for the initial CV dye (peak A), the peaks initially increase before subsequently decreasing, indicating the formation and transformation of intermediates.

In Fig. S15 of the ESI,† the maximum absorption of the spectral bands shifts from 588.5 nm (spectrum A) to 541.5 nm (spectrum J), from 377.0 nm (spectrum a) to 339.0 nm (spectrum f), and from 309.1 nm (spectrum α) to 278.3 nm (spectrum γ). The maximum adsorption in the visible and ultraviolet spectral region of each intermediate is depicted in Table S3.† They are identified as A–J a–f, and α–γ, respectively corresponding to the peaks A–J, a–f, and α–γ in Fig. S14 (ESI†). These shifts of the absorption band are presumed to result from the formation of a series of *N*-de-methylated intermediates. From these results, several families of intermediates could be distinguished. The intermediates were further identified using the HPLC-ESI mass spectrometric method, and the relevant mass spectra are illustrated in Fig. S16 and Table S3 (ESI†). The molecular ion peaks appear in the acid forms of the intermediates. The detailed data of the intermediates are described in the ESI.†

3.9 Mechanism of the photocatalytic degradation of CV

Generally speaking, three possible reaction mechanisms are suspected to be involved in dye photodegradation by a

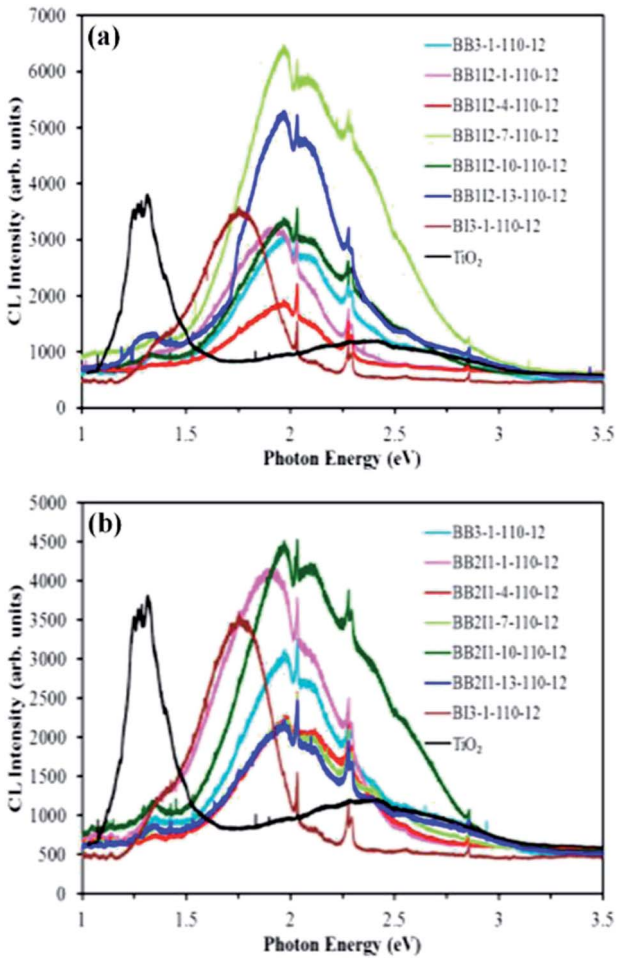

Fig. 9 Photoluminescence spectra of TiO_2, BiOBr, BiOI, and BiO_pBr_q/BiO_mI_n. Molar ratio KBr/KI (a) 1/2, (b) 2/1.

semiconductor, namely (i) a photolysis process, (ii) a dye photosensitization process, and (iii) a photocatalytic process.[25] In this experiment, CV degradation by the photolysis process upon visible light irradiation in the blank experiment was not observable.

In this study, slight changes in the CV concentration over different samples can be detected during 30 min of a dark adsorption experiment before the photocatalytic reactions. The slight CV adsorption on the catalyst benefits the transfer of charge carriers between the dye and the catalyst surfaces in the dye photosensitization process. Presuming that the photosensitization process takes place with BiO_pBr_q/BiO_mI_n, that is to say, the photosensitization mechanism in the CV decomposition can not be neglected.

As is known, various primary reactive species, such as the hydroxyl radical HO$^{\bullet}$, photogenerated hole h^+, superoxide radical $O_2^{-\bullet}$ and singlet oxygen $^1O_2$, can be formed during the photocatalytic degradation process in the UV-vis/semiconductor system.[6,7,26,27] Shenawi-Khalil and his coworkers showed that the rhodamine-B and acetophenone photodegradation by BiOCl-bismuth oxyhydrate under visible light was dominated by $O_2^{-\bullet}$ and h^+ oxidation as the main active species.[25] Chen *et al.* proposed a pathway for generating active oxygen radicals ($^{\bullet}$OH) on the surface of $Bi_2O_2CO_3$/BiOI for the degradation of dye.[28] Xiao's group revealed that highly efficient visible-light-driven bisphenol-A removal with BiOBr/BiOI could be attributed to effective separation and transfer of the photoinduced charge carriers in BiOBr/BiOI with a narrower band gap and more negative conduction band position, which favored the photogenerated holes.[23] Wang *et al.* reported that $^{\bullet}$OH radicals were generated by the multistep reduction of $O_2^{-\bullet}$.[29] Therefore, photogenerated holes on the surface of bismuth oxyhalides were not expected to react with OH^-/H_2O to form $^{\bullet}$OH, suggesting that the decomposition of bisphenol-A[18] and rhodamine[27] could be attributed to a direct reaction with the photogenerated holes or with the superoxide radical or both species.

In order to evaluate the effect of the active species during the photocatalytic reaction, a series of quenchers were introduced to scavenge the relevant active species. $O_2^{-\bullet}$, $^{\bullet}$OH, h^+, and $^1O_2$ were investigated by adding 1.0 mM benzoquinone,[30] isopropanol,[31] ammonium oxalate,[32] and sodium azide,[33] respectively. As shown in Fig. 10(a), the degradation efficiency of IPA quenching decreased more than that of AO, and the degradation efficiency of BQ quenching decreased more than that of

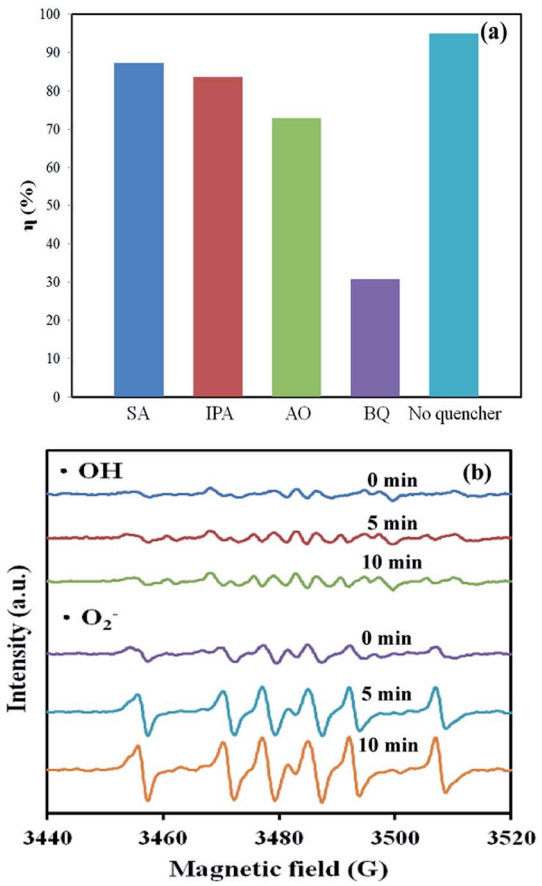

Fig. 10 (a) The dye concentration during photodegradation as a function of irradiation time observed in BiO_pBr_q/BiO_mI_n under the addition of different scavengers: SA, IPA, AQ, and BQ. (b) DMPO spin-trapping EPR spectra for DMPO–O_2^- and DMPO–OH under visible light irradiation with BiO_xCl_y/BiO_mI_n.

IPA, but the photocatalytic degradation of CV was not affected by the addition of SA. In short, the quenching effects of various scavengers showed that the reactive $O_2^{\bullet -}$ played a major role, and $^{\bullet}OH$ or h^+ played a minor role in the CV degradation. From Fig. 10(b), the six characteristic peaks of the DMPO–O_2^- adducts were observed in the visible light irradiated BiO_pBr_q/BiO_mI_n dispersions. But, the four characteristic peaks of DMPO–OH adducts (1 : 2:2 : 1 quartet pattern) were not observed in visible light irradiated BiO_pBr_q/BiO_mI_n aqueous dispersions. Fig. 10(b) indicated that no EPR signals were observed when the reaction was performed in the dark, while the signals with intensities corresponding to the characteristic peaks of DMPO–O_2^- adducts[34] were observed during the reaction process under visible light irradiation, and the intensity gradually increased with the prolonged reaction time, suggesting that $O_2^{\bullet -}$ (the major active species) has been formed in the presence of BiO_pBr_q/BiO_mI_n and oxygen under visible light irradiation.

Wang *et al.* reported that $^{\bullet}OH$ radicals were generated by the multistep reduction of $O_2^{\bullet -}$.[29] However, photogenerated holes on the surface of bismuth oxyhalides were not expected to react with OH^-/H_2O to form $^{\bullet}OH$, suggesting that the decomposition of bisphenol-A[18] and rhodamine[27] could be attributed to a direct reaction with the photogenerated holes or with superoxide radical or both species. Therefore, the $O_2^{\bullet -}$ radical is the most important active species in the photocatalytic degradation of CV or phenol by BiO_xCl_y/BiO_mI_n.

Chen *et al.* reported[35] that Pt–TiO_2 accumulated less negative species on catalyst surfaces, which deteriorated reaction rates, than pure TiO_2 did in an acidic environment. The $^{\bullet}OH$ radical is produced subsequently, as also shown in eqn (19)–(24).

$$O_2^{\bullet -} + H^+ + e^- \rightarrow HOO^{\bullet} \quad (19)$$

$$HOO^{\bullet} + H_2O \rightarrow {}^{\bullet}OH + H_2O_2 \quad (20)$$

$$O_2^{\bullet -} + 2H^+ \rightarrow H_2O_2 \quad (21)$$

$$H_2O_2 + e^- \rightarrow {}^{\bullet}OH + OH^- \quad (22)$$

$$h^+ + OH^- \rightarrow {}^{\bullet}OH \quad (23)$$

$$h^+ + H_2O \rightarrow {}^{\bullet}OH + H^+ \quad (24)$$

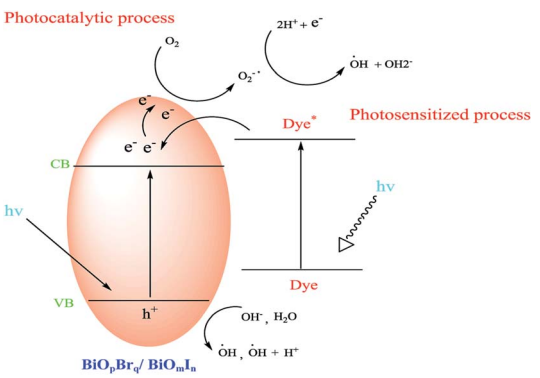

Fig. 11 The band structure diagram of the BiO_pBr_q/BiO_mI_n nanocomposites and the possible charge separation processes.

These cycles continuously occur when the system is exposed to visible light irradiation. Finally, after several cycles of photo-oxidation, the degradation of CV by the formed oxidant species can be expressed by eqn (25)–(27).

$$CV + h^+ \rightarrow CV^{+\bullet} \rightarrow \text{degraded compounds} \quad (25)$$

$$CV + {}^{\bullet}OH / O_2^{-\bullet} \rightarrow \text{degraded compounds} \quad (26)$$

$$CV^{+\bullet} + {}^{\bullet}OH / O_2^{-\bullet} \rightarrow \text{degraded compounds} \quad (27)$$

It has been reported that some dyes exhibit a dye sensitized degradation mechanism.[36] This photocatalytic degradation is also attributed to the photodegradation of CV through the photocatalytic pathway of CV photosensitized BiO_pBr_q/BiO_mI_n. CV absorbs a visible photon and is promoted to an excited electronic state CV*, from which an electron can be transferred into the conduction band of BiO_pBr_q/BiO_mI_n:

$$CV + h\nu \rightarrow CV^* \quad (28)$$

$$CV^* + BiO_pBr_q/BiO_mI_n \rightarrow CV^{+\bullet} + BiO_pBr_q/BiO_mI_n\ (e^-) \quad (29)$$

$$O_2 + e^- \rightarrow O_2^{-\bullet} \quad (30)$$

Once the electron reaches the BiO_pBr_q/BiO_mI_n conduction band, it subsequently induces the generation of active oxygen species (eqn (30), (19)–(22)), which result in the degradation of CV. Clearly, apart from the photodegradation of CV through the pathway of BiO_pBr_q/BiO_mI_n-mediated and photosensitized processes, there is another kind of photocatalytic pathway to account for the enhanced photocatalytic activity. Both the photocatalytic process and the photosensitized process would work concurrently, as shown in Fig. 11.

In earlier reports,[5,35,37–39] the *N*-de-alkylation processes were preceded by the formation of a nitrogen-centered radical while the destruction of dye chromophore structures was preceded by the generation of a carbon-centered radical in the photocatalytic degradation of triphenylmethane dyes. On the basis of the above experimental results, a dye degradation mechanism is tentatively proposed, as depicted in Fig. S17–S19 (ESI†).

4. Conclusions

In the current process, the controllable crystal phases and morphologies of bismuth oxybromides/bismuth oxyiodides could be accomplished by simply changing some growth parameters, including the molar ratio (Br/I), pH value, and reaction temperature. The increased photocatalytic activities of BiO_pBr_q/BiO_mI_n could be attributed to the formation of the heterojunction between BiO_pBr_q and BiO_mI_n, which effectively suppresses the recombination of photoinduced electron–hole pairs. Both the photocatalytic process and the photosensitized process work concurrently. $O_2^{\bullet -}$ is the main active species and h^+ and $^{\bullet}OH$ are two minor active species in the whole process while $^1O_2$ can be negligible. The reaction mechanisms for vis/BiO_pBr_q/BiO_mI_n proposed in this study should offer some

insight for the future development of technology applications for the degradation of dyes.

Acknowledgements

This research was supported by the Ministry of Science and Technology of the Republic of China (NSC-101-2113 M- 142-001-MY3).

Notes and references

1 C. J. Brinker, B. Cornils and M. Bonet, *Triarylmethane and Diarylmethane Dyes*, Wiley-VCH, New York, 6th edn, 2001.
2 L. M. Lewis and G. L. Indig, *J. Photochem. Photobiol., B*, 2002, **67**, 139–148.
3 B. P. Cho, T. Yang, L. R. Blankenship, J. D. Moody, M. Churchwell, F. A. Bebland and S. J. Culp, *Chem. Res. Toxicol.*, 2003, **16**, 285–294.
4 K. Yu, S. G. Yang, C. Liu, H. Chen, H. Li, C. Sun and A. B. Stephen, *Environ. Sci. Technol.*, 2012, **46**, 7318–7326.
5 Y. H. Liao, J. X. Wang, J. S. Lin, W. H. Chung, W. Y. Lin and C. C. Chen, *Catal. Today*, 2011, **174**, 148–159.
6 Y. Zhang, N. Zhang, Z. R. Tang and Y. J. Xu, *Chem. Sci.*, 2012, **3**, 2812–2822.
7 M. Q. Yang, Y. Zhang, N. Zhang, Z. R. Tang and Y. J. Xu, *Sci. Rep.*, 2013, **3**, 3314.
8 M. Q. Yang, N. Zhang, M. Pagliaro and Y. J. Xu, *Chem. Soc. Rev.*, 2014, **43**, 8240–8254.
9 N. Zhang, Y. Zhang and Y.-J. Xu, *Nanoscale*, 2012, **4**, 5792–5813.
10 N. Zhang, M. Q. Yang, Z. R. Tang and Y. J. Xu, *ACS Nano*, 2014, **8**, 623–633.
11 Y. Zhang, Z. R. Tang, X. Fu and Y. J. Xu, *ACS Nano*, 2010, **4**, 7303–7311.
12 C. Han, M. Q. Yang, B. Weng and Y. J. Xu, *Phys. Chem. Chem. Phys.*, 2014, **16**, 16891–16903.
13 W. W. Lee, C. S. Lu, C. W. Chuang, Y. J. Chen, J. Y. Fu, C. W. Siao and C. C. Chen, *RSC Adv.*, 2015, **5**, 23450–23463.
14 L. Ye, J. Chen, L. Tian, J. Liu, T. Peng, K. Deng and L. Zan, *Appl. Catal., B*, 2013, **130–131**, 1–7.
15 Y. R. Jiang, H. P. Lin, W. H. Chung, Y. M. Dai, W. Y. Lin and C. C. Chen, *J. Hazard. Mater.*, 2015, **283**, 787–805.
16 S. T. Huang, Y. R. Jiang, S. Y. Chou, Y. M. Dai and C. C. Chen, *J. Mol. Catal. A: Chem.*, 2014, **391**, 105–120.
17 S. Shenawi-Khalil, V. Uvarov, S. Fronton, I. Popov and Y. Sasson, *Appl. Catal., B*, 2012, **117–118**, 148–155.
18 X. Xiao, R. Hao, M. Liang, X. Zuo, J. Nan, L. Li and W. Zhang, *J. Hazard. Mater.*, 2012, **233–234**, 122–130.
19 J. Cao, B. Xu, B. Luo, H. Lin and S. Chen, *Catal. Commun.*, 2011, **13**, 63–68.
20 X. Xiao, R. Hao, X. Zuo, J. Nan, L. Li and W. Zhang, *Chem. Eng. J.*, 2012, **209**, 293–300.
21 X. Xiao and W. D. Zhang, *RSC Adv.*, 2011, **1**, 1099–1105.
22 J. Zhang, F. Shi, J. Lin, D. Chen, J. Gao, Z. Huang, X. Ding and C. Tang, *Chem. Mater.*, 2008, **20**, 2937–2941.
23 J. Wang, Y. Yu and L. Zhang, *Appl. Catal., B*, 2013, **136–137**, 112–121.
24 W. D. Wang, F. Q. Huang and X. P. Lin, *Scr. Mater.*, 2007, **56**, 669–672.
25 S. K. Sanaa, U. Vladimir, M. Ella, P. Inna and S. Yoel, *Appl. Catal., A*, 2012, **413–414**, 1–9.
26 X. Xiao, R. Hu, C. Liu, C. Xing, X. Zuo, J. Nan and L. Wang, *Chem. Eng. J.*, 2013, **225**, 790–797.
27 S. K. Sana, U. Vladimir, F. Sveta, P. Inna and S. Yoel, *Appl. Catal., B*, 2012, **117–118**, 148–155.
28 L. Chen, S. F. Yin, S. L. Luo, R. Huang, Q. Zhang, T. Hong and P. C. T. Au, *Ind. Eng. Chem. Res.*, 2012, **51**, 6760–6768.
29 J. Wang, Y. Yu and L. Zhang, *Appl. Catal., B*, 2013, **136–137**, 112–121.
30 M. C. Yin, Z. S. Li, J. H. Kou and Z. G. Zou, *Environ. Sci. Technol.*, 2009, **43**, 8361–8366.
31 L. S. Zhang, K. H. Wong, H. Y. Yip, C. Hu, J. C. Yu, C. Y. Chan and P. K. Wong, *Environ. Sci. Technol.*, 2010, **44**, 1392–1398.
32 S. G. Meng, D. Z. Li, M. Sun, W. J. Li, J. X. Wang, J. Chen, X. Z. Fu and G. C. Xiao, *Catal. Commun.*, 2011, **12**, 972–975.
33 G. Li, K. H. Wong, X. Zhang, C. Hu, J. C. Yu, R. C. Y. Chan and P. K. Wong, *Chemosphere*, 2009, **76**, 1185–1191.
34 X. Xiao, C. Xing, G. He, X. Zuo, J. Nan and L. Wang, *Appl. Catal., B*, 2014, **148–149**, 154–163.
35 H. J. Fan, C. S. Lu, W. L. W. Lee, M. R. Chiou and C. C. Chen, *J. Hazard. Mater.*, 2011, **185**, 227–235.
36 X. Zhu, J. Zhang and F. Chen, *Appl. Catal., B*, 2011, **102**, 316–322.
37 H. P. Lin, J. Y. Chen, W. H. Lien and C. C. Chen, *J. Taiwan Inst. Chem. Eng.*, 2014, **45**, 2469–2479.
38 K. L. Li, W. W. Lee, C. S. Lu, Y. M. Dai, S. Y. Chou, M. C. Wang and C. C. Chen, *J. Taiwan Inst. Chem. Eng.*, 2014, **45**, 2688–2697.
39 H. L. Chen, W. W. Lee, W. H. Chung, Y. J. Chen, Y. R. Jiang, H. P. Lin, W. Y. Lin and C. C. Chen, *J. Taiwan Inst. Chem. Eng.*, 2014, **45**, 1892–1909.

